

Antisite Pairs Suppress the Thermal Conductivity of BAs

Qiang Zheng,¹ Carlos A. Polanco,¹ Mao-Hua Du,¹ Lucas R. Lindsay,¹ Miaofang Chi,² Jiaqiang Yan,^{1,3} and Brian C. Sales¹

¹Materials Science and Technology Division, Oak Ridge National Laboratory, Oak Ridge, Tennessee 37831, USA

²Center for Nanophase Materials Sciences, Oak Ridge National Laboratory, Oak Ridge, Tennessee 37831, USA

³Department of Materials Science and Engineering, University of Tennessee, Knoxville, Tennessee 37996, USA



(Received 6 February 2018; published 6 September 2018)

BAs was predicted to have an unusually high thermal conductivity with a room temperature value of $2000 \text{ W m}^{-1} \text{ K}^{-1}$, comparable to that of diamond. However, the experimentally measured thermal conductivity of BAs single crystals is still lower than this value. To identify the origin of this large inconsistency, we investigate the lattice structure and potential defects in BAs single crystals at the atomic scale using aberration-corrected scanning transmission electron microscopy (STEM). Rather than finding a large concentration of As vacancies (V_{As}), as widely thought to dominate the thermal resistance in BAs, our STEM results show an enhanced intensity of some B columns and a reduced intensity of some As columns, suggesting the presence of antisite defects with As_{B} (As atom on a B site) and B_{As} (B atom on an As site). Additional calculations show that the antisite pair with As_{B} next to B_{As} is preferred energetically among the different types of point defects investigated and confirm that such defects lower the thermal conductivity for BAs. Using a concentration of 1.8(8)% ($6.6 \pm 3.0 \times 10^{20} \text{ cm}^{-3}$ in density) for the antisite pairs estimated from STEM images, the thermal conductivity is estimated to be $65\text{--}100 \text{ W m}^{-1} \text{ K}^{-1}$, in reasonable agreement with our measured value. Our study suggests that $\text{As}_{\text{B}}\text{-B}_{\text{As}}$ antisite pairs are the primary lattice defects suppressing thermal conductivity of BAs. Possible approaches are proposed for the growth of high-quality crystals or films with high thermal conductivity. Employing a combination of state-of-the-art synthesis, STEM characterization, theory, and physical insight, this work models a path toward identifying and understanding defect-limited material functionality.

DOI: [10.1103/PhysRevLett.121.105901](https://doi.org/10.1103/PhysRevLett.121.105901)

As microelectronic devices develop towards miniaturization and faster processing, thermal management plays a crucial role in the design of electronics packaging. Therefore, materials with a high thermal conductivity (κ) are becoming increasingly essential for new-generation electronic devices [1]. Recently, cubic boron arsenide (BAs) was predicted to possess an exceptionally high κ over $2000 \text{ W m}^{-1} \text{ K}^{-1}$ at room temperature based on first-principles calculations [2,3], comparable to that of diamond. The high κ in BAs is attributed to the combination of a large acoustic-optic frequency gap and a bunching of the acoustic phonon dispersions, which significantly reduce phonon-phonon scattering [2–4]. This remarkably high κ attracted intense attention; however, the experimental values for κ are still below the predicted one [5–10]. While previous *ab initio* calculations [11] and x-ray photoelectron spectroscopy studies [5,6] suggested that As vacancies, even with very low concentrations, could effectively suppress κ , there has been no direct observation of As vacancies in BAs crystals or films, and the real cause of the suppression of κ remains unclear. Identifying the defects that suppress κ could provide effective guidance for the growth of defect-free BAs crystals or films with further greatly improved κ and future applications of this material. Since lattice defects are, in general, quite local, atomic-

scale scanning transmission electron microscopy (STEM) is a powerful tool for such investigations.

In this Letter, we investigate possible defects in BAs single crystals at the atomic scale utilizing aberration-corrected STEM combined with density-functional theory (DFT) calculations. $\text{As}_{\text{B}}\text{-B}_{\text{As}}$ antisite pairs are identified as the primary lattice defects suppressing the thermal conductivity of BAs. Using a concentration of 1.8(8)% ($6.6 \pm 3.0 \times 10^{20} \text{ cm}^{-3}$ in density) for the antisite pairs estimated from STEM images, the thermal conductivity is estimated to be $65\text{--}100 \text{ W m}^{-1} \text{ K}^{-1}$, comparable to our measured value.

BAs single crystals were grown by the vapor transport method using iodine as the transport agent [12]. The room temperature κ of as-grown single crystals was measured to be $\sim 140 \text{ W m}^{-1} \text{ K}^{-1}$ [13], comparable to the values reported by other groups [5,6]. STEM specimens were prepared by crushing BAs crystals. The STEM experiments were performed in an aberration-corrected Nion UltraSTEM 100TM, operating at 100 kV accelerating voltage [14]. High-angle annular dark-field (HAADF) images were collected with a probe convergence angle of 30 mrad and an inner collection angle of 86 mrad. The thickness for each imaging region was measured from the corresponding electron energy loss (EEL) spectrum using

the log-ratio method with an inelastic mean free path (λ) calculation as described in Refs. [15,16].

BAs crystallizes in a zinc blende cubic structure with space group $F\bar{4}3m$ and lattice parameter $a = 4.7776 \text{ \AA}$ [17]. As shown in Fig. 1(a), its perfect structure in the projection of [001] reveals each atomic column involving a single type of atoms, either B or As. Figure 1(b) displays a typical HAADF image along [001] for a region with a thickness of $\sim 1.7 \text{ nm}$ ($\sim 3.6a$), as measured from the corresponding EEL spectrum [Fig. 1(c)]. In most areas of Fig. 1(b), only As columns show visible intensities, which are as expected, since the HAADF image intensity is roughly proportional to Z^2 (Z is the atomic number), and, thus, in the perfect structure the intensities of B columns should be negligible compared to those of As columns. However, obvious intensities for some B columns and intensity weakening for some As columns are observed as highlighted by the intensity profile in Fig. 1(d), indicating the appearance of As atoms on B sites (As_B antisites) and B atoms on As sites (B_{As} antisites) or As vacancies (V_{As}).

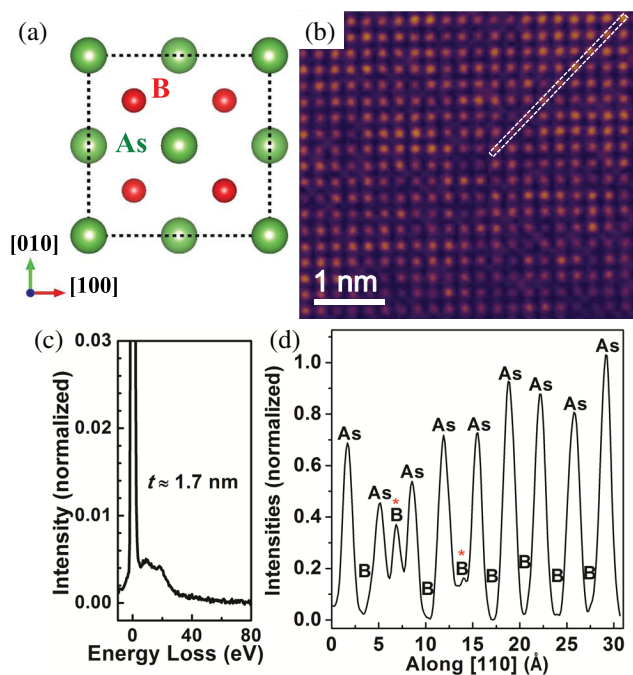


FIG. 1. (a) The crystal structure of BAs in the projection of [001]. Note that each atomic column along this direction is constructed of atoms of a single type. (b) A HAADF image along [001] for a region with a thickness of 1.7 nm (~ 3.6 unit cells). The thickness for this region was calculated from its EEL spectrum in (c). The intensity profile for the dashed rectangular region in (b) is displayed in (d), revealing As_B antisite defects and intensity weakening for their neighboring As columns. The intensities of the two B columns marked by red asterisks in (d) are 0.38 and 0.19, respectively, revealing 1As_B in each of them, and the intensity difference between them is due to probe channeling (see details in Fig. S3 in Supplemental Material [18]).

Note that crystals were grown starting with high-purity As and B materials, and no foreign atoms were observed by elemental analysis and EEL spectroscopy measurements for the detected areas (see Fig. S1 [18]). To assess the possible effects of the crystal edge, a much thicker region (with a thickness of $\sim 4.7 \text{ nm}$) far away from the edge was chosen for HAADF imaging (see Fig. S2 [18]), and similar features were also observed.

Image simulations were then performed to better visualize the intensity variations caused by possible As_B in B columns and B_{As} or V_{As} in As columns (See Supplemental Material for more details [18]). Simulations of the intensity profile with the intensity of a pristine As column normalized to 1 suggest that the intensity of a B column with 1As_B could vary between 0.18 and 0.4, while that of an As column with 1B_{As} or $1V_{As}$ could be in the range of 0.55 and 0.94, due to probe channeling [20]. We then measured intensities for the visible B columns in Fig. 1(b) and other images with the same thicknesses. As exemplified by two B columns containing As_B antisite defects marked by red asterisks in Fig. 1(d), the intensities of almost all visible B columns are between 0.18 and 0.4, much weaker than the simulated intensities for a B column with 2As_B (0.69–0.84) or 3As_B (0.87–0.93) (see Fig. S4 [18]), suggesting only one As_B antisite defect in each of them. By counting the As_B defects in over ten HAADF images of different regions with comparable thicknesses as in Fig. 1(b), the concentration was estimated to be 1.8(8)% ($6.6 \pm 3.0 \times 10^{20} \text{ cm}^{-3}$ in density). The large error bar comes from the fact that the concentration estimation at very thin regions is affected by various facts such as the type of atoms on the top and bottom surfaces.

Although the HAADF imaging and simulations strongly suggest the presence of As_B antisite defects in BAs, we cannot distinguish the origin of the reduced intensity on the As columns directly, whether the intensity drop is due to B_{As} or V_{As} . We thus carefully analyzed the local area variation in HAADF images. As shown in Figs. 1(b) and 1(d), B columns with enhanced intensities are always found neighboring to As columns with reduced intensities, indicating pairing of B_{As} and As_B antisite defects in the structure. We also performed a careful search of other types of defects, with special attention paid to As vacancies, which have been widely believed to suppress κ of BAs. However, we did not find any trace of them with a comparable concentration to that of the B_{As} - As_B pairs. The defect formation energy calculations discussed below show B_{As} - As_B pairs are the most energetically preferred.

To further understand the origin of this particular defect type in BAs, the formation energies of different types of defects are calculated (See Supplemental Material for detailed computational methods [18]). Figure 2 shows the calculated formation energies of native point defects (vacancies, interstitials, and antisites) in BAs. The Fermi level is pinned approximately at the crossing point between

the formation energy lines of the lowest-energy donor (V_B^+) and acceptor (B_{As}^{2-}) defects (indicated by the vertical dotted line in Fig. 2). At this Fermi level, the antisite pair As_B-B_{As} has the lowest formation energy (1.95 eV) among all native point defects, consistent with the STEM result. However, the calculated thermal-equilibrium concentration of As_B-B_{As} (density on the order of 10^{13} cm^{-3}) at the growth temperature of 850°C [using Eq. (5) in Supplemental Material [18]] is significantly lower than that observed in HAADF images. The high defect formation energies indicate strong covalent bonding in BAs, which is consistent with the predicted high thermal conductivity. The high concentration of antisite defects as seen in HAADF images is likely because thermal equilibrium is not reached during crystal growth. The gas-phase species react to form solid-state BAs in the vapor transport synthesis. It is likely that a large number of antisite pairs are trapped in the crystal lattice. Thermal annealing is supposed to reduce the defect concentration to its thermal-equilibrium value provided that sufficient atomic diffusion can take place. However, the atomic diffusion in BAs is likely limited especially for As even at the growth temperature of 850°C for the following reasons: (i) The As interstitial (As_i) and As vacancy (V_{As}) defects both have very high formation energies as shown in Fig. 2. Thus, the concentrations of As_i and V_{As} are likely orders of magnitudes lower than that of As_B-B_{As} regardless of whether thermal equilibrium can be reached. (ii) BAs has a small lattice constant but a large size mismatch between B and As. As a result, the diffusion of the large As_i interstitial is likely difficult. The diffusion of V_{As} involves creating two V_{As} and one As_i at the transition

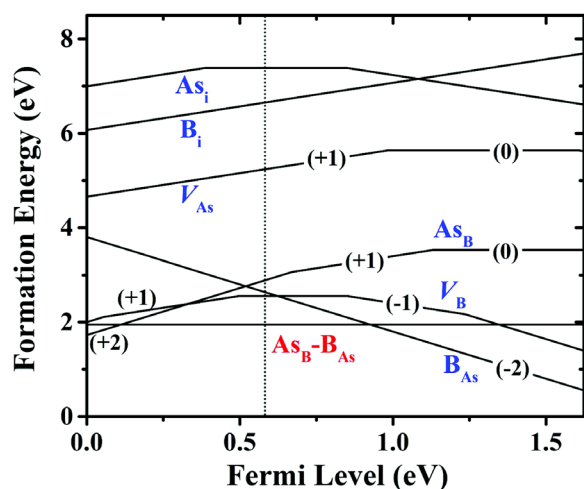


FIG. 2. Formation energies of native point defects (including vacancies, interstitials, and antisites; the red label is for the $B_{As}-As_B$ pair) in BAs as a function of the Fermi level. The slope of the formation energy line indicates the charge state of the defect. The Fermi level is pinned approximately at the crossing point between the formation energy lines of the lowest-energy donor (V_B^+) and acceptor (B_{As}^{2-}) defects (indicated by the dotted line).

state of the diffusion path, which may lead to a high diffusion barrier, because both V_{As} and As_i have very high formation energies. Thus, the low concentration and high diffusion barrier of As_i and V_{As} may severely limit As diffusion in BAs. This prevents the As_B-B_{As} defect from reaching its thermal equilibrium, thereby trapping a substantial amount of As_B-B_{As} defects in BAs as seen in HAADF images.

Extrinsic thermal resistance in a material with extended and point defects becomes significant as intrinsic anharmonic resistance becomes weak, e.g., with a decreasing temperature. For high thermal conductivity (κ) materials, this can be exaggerated, as is the case for diamond and graphene, where phonon-isotope scattering has been shown to reduce their κ by more than 50% even at room temperature [39,40]. In BAs with predicted $\kappa > 2000 \text{ W m}^{-1} \text{ K}^{-1}$ [2], phonon-defect scattering may also be extremely important, especially in validating the prediction by experiment. Previous theoretical work demonstrated that 0.004% As vacancies ($\sim 1.5 \times 10^{18} \text{ cm}^{-3}$) reduce the predicted κ by half [11]. Thus, the large concentration of antisite defects observed here is likely a leading factor in the much reduced thermal conductivity observed experimentally, $\kappa \sim 140 \text{ W m}^{-1} \text{ K}^{-1}$ [13]. Figure 3 shows κ of BAs calculated using the full solution of the Peierls-Boltzmann transport equation for three-phonon scattering with first-principles interatomic force constants [31–33]. A parameter-free *ab initio* Green's function methodology [11,34,35], which has demonstrated good agreement with measured κ data [41,42], was used to include phonon-defect scattering from different defect types with varying concentrations (see Supplemental Material [18]). Using the estimated density of As_B-B_{As} pairs from the STEM measurements here ($6.6 \pm 3.0 \times 10^{20} \text{ cm}^{-3}$), calculations give a κ of $65\text{--}100 \text{ W m}^{-1} \text{ K}^{-1}$, comparable to the measured value.

The identification of As_B-B_{As} pairs as the primary defects suppressing κ of BAs and the high formation energy from DFT calculations provide important information and highlight the importance of kinetic factors during synthesizing high-quality BAs materials with a predicted high κ . Tuning the pressure and/or temperature might change both the chemical potential of vapor species inside of the growth ampoule and the growth kinetics in vapor transport synthesis. Chemical vapor transport growth starting with BAs or BP seeds seems to facilitate the nucleation process and deserves further study [7–9]. Growth of BAs crystals out of flux might be another promising approach, though challenging due to the limited solubility of B in most low-melting fluxes. A thorough investigation of phase diagrams suggests Ni- or alkali-metal-based fluxes are promising with a reasonable solubility of B [43–46]. Considering the growth of $B_{12}As_2$ out of NiB melt [47], the B content in the Ni-based flux should be carefully controlled, and an As-rich Ni-based flux is recommended to avoid the precipitation of $B_{12}As_2$. For the growth of

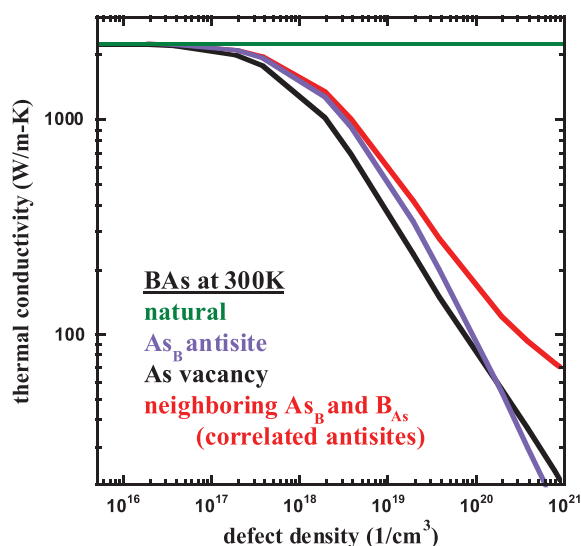


FIG. 3. Calculated thermal conductivity (κ) of BAs at room temperature for As_B antisite defects (blue curve), As vacancies (black curve), and neighboring As_B and B_{As} antisite defects (red curve) as a function of the defect density. The horizontal green line gives the room temperature calculated κ for BAs with natural isotope variation and three-phonon scattering.

high-quality BAs films, molecular beam epitaxy (MBE) might be a good option.

In summary, with a combined effort of STEM imaging and DFT calculations, we identify that As_B - B_{As} antisite pairs are the primary lattice defects, rather than As vacancies, suppressing the thermal conductivity of BAs single crystals. Further studies are needed to understand the kinetic factors leading to the formation of these lattice defects during vapor transport growth. Flux growth out of alkali-metal-based or Ni-based melts might be a good option for high-quality crystals. Considering the sensitivity of thermal conductivity to lattice defects, MBE is suggested for the growth of BAs films.

This work was supported by the U.S. Department of Energy (DOE), Office of Science, Basic Energy Sciences (BES), Materials Sciences and Engineering Division. The electron microscopy in this work was conducted at the ORNL's Center for Nanophase Materials Sciences (CNMS), which is a DOE Office of Science User Facility. C. A. P. and L. R. L. acknowledge computational resources from the National Energy Research Scientific Computing Center (NERSC), a DOE Office of Science User Facility supported by the Office of Science of the U.S. Department of Energy under Contract No. DE-AC02-05CH11231. Q. Z. thanks E.-J. Guo for helpful discussions. This manuscript has been authored by UT-Battelle, LLC under Contract No. DE-AC05-00OR22725 with the U.S. Department of Energy. The United States Government retains and the publisher, by accepting the article for publication, acknowledges that the United States

Government retains a non-exclusive, paid-up, irrevocable, world-wide license to publish or reproduce the published form of this manuscript, or allow others to do so, for United States Government purposes. The Department of Energy will provide public access to these results of federally sponsored research in accordance with the DOE Public Access Plan [48].

Note added.—Recently, we became aware of three papers published in Science [8–10] that reported the growth of single crystals of BAs with thermal conductivity values near $1000 \text{ W m}^{-1} \text{ K}^{-1}$. Based on our findings, these new crystals presumably have fewer antisite-pair defects as compared to previous work [5–7].

- [1] A. L. Moore and L. Shi, *Mater. Today* **17**, 163 (2014).
- [2] L. Lindsay, D. A. Broido, and T. L. Reinecke, *Phys. Rev. Lett.* **111**, 025901 (2013).
- [3] D. A. Broido, L. Lindsay, and T. L. Reinecke, *Phys. Rev. B* **88**, 214303 (2013).
- [4] H. Ma, C. Li, S. Tang, J. Yan, A. Alatas, L. Lindsay, B. C. Sales, and Z. Tian, *Phys. Rev. B* **94**, 220303 (2016).
- [5] J. Kim, D. A. Evans, D. P. Sellan, O. M. Williams, E. Ou, A. H. Cowley, and L. Shi, *Appl. Phys. Lett.* **108**, 201905 (2016).
- [6] B. Lv, Y. Lan, X. Wang, Q. Zhang, Y. Hu, A. J. Jacobson, D. Broido, G. Chen, Z. Ren, and C.-W. Chu, *Appl. Phys. Lett.* **106**, 074105 (2015).
- [7] F. Tian, B. Song, B. Lv, J. Sun, S. Huyan, Q. Wu, J. Mao, Y. Ni, Z. Ding, S. Huberman, T.-H. Liu, G. Chen, S. Chen, C.-W. Chu, and Z. Ren, *Appl. Phys. Lett.* **112**, 031903 (2018).
- [8] J. S. Kang, M. Li, H. Wu, H. Nguyen, and Y. Hu, *Science* **361**, 575 (2018).
- [9] F. Tian, B. Song, X. Chen, N. K. Ravichandran, Y. Lv, K. Chen, S. Sullivan, J. Kim, Y. Zhou, T.-H. Liu, M. Goni, Z. Ding, J. Sun, G. A. G. U. Gamage, H. Sun, H. Ziyae, S. Huyan, L. Deng, J. Zhou, A. J. Schmidt *et al.*, *Science* **361**, 582 (2018).
- [10] S. Li, Q. Zheng, Y. Lv, X. Liu, X. Wang, P. Y. Huang, and D. G. Cahill, *Science* **361**, 579 (2018).
- [11] N. H. Protik, J. Carrete, N. A. Katcho, N. Mingo, and D. Broido, *Phys. Rev. B* **94**, 045207 (2016).
- [12] T. L. Chu and A. E. Hyslop, *J. Appl. Phys.* **43**, 276 (1972).
- [13] J.-Q. Yan (unpublished).
- [14] O. Krivanek, G. Corbin, N. Dellby, B. Elston, R. Keyse, M. Murfitt, C. Own, Z. Szilagy, and J. Woodruff, *Ultramicroscopy* **108**, 179 (2008).
- [15] T. Malis, S. C. Cheng, and R. F. Egerton, *Microsc. Res. Tech.* **8**, 193 (1988).
- [16] R. Egerton, *Electron Energy-Loss Spectroscopy in the Electron Microscope* (Springer, New York, 2011).
- [17] J. A. Perri, S. La Placa, and B. Post, *Acta Crystallogr.* **11**, 310 (1958).
- [18] See Supplemental Material at <http://link.aps.org/supplemental/10.1103/PhysRevLett.121.105901> for an SEM image, an EXD spectrum and an EEL spectrum for

- a BAs single crystal, more STEM imaging and simulation, and details on computational methods for defect formation energies and thermal conductivity, which includes Refs. [11,17,19–38].
- [19] C. Koch, QSTEM (2008).
- [20] B. D. Esser, A. J. Hauser, R. E. A. Williams, L. J. Allen, P. M. Woodward, F. Y. Yang, and D. W. McComb, *Phys. Rev. Lett.* **117**, 176101 (2016).
- [21] J. Hwang, J. Y. Zhang, A. J. D'Alfonso, L. J. Allen, and S. Stemmer, *Phys. Rev. Lett.* **111**, 266101 (2013).
- [22] M. Haruta, H. Kurata, H. Komatsu, Y. Shimakawa, and S. Isoda, *Ultramicroscopy* **109**, 361 (2009).
- [23] G. Kresse and J. Furthmüller, *Comput. Mater. Sci.* **6**, 15 (1996).
- [24] G. Kresse and D. Joubert, *Phys. Rev. B* **59**, 1758 (1999).
- [25] J. P. Perdew, K. Burke, and M. Ernzerhof, *Phys. Rev. Lett.* **77**, 3865 (1996).
- [26] J. Heyd, G. E. Scuseria, and M. Ernzerhof, *J. Chem. Phys.* **118**, 8207 (2003).
- [27] A. V. Krukau, O. A. Vydrov, A. F. Izmaylov, and G. E. Scuseria, *J. Chem. Phys.* **125**, 224106 (2006).
- [28] K. Biswas, M.-H. Du, and D. J. Singh, *Phys. Rev. B* **86**, 144108 (2012).
- [29] S. Lany and A. Zunger, *Phys. Rev. B* **78**, 235104 (2008).
- [30] A. Ektarawong, S. I. Simak, and B. Alling, *Phys. Rev. B* **96**, 024202 (2017).
- [31] J. M. Ziman, *Electrons and Phonons: The Theory of Transport Phenomena in Solids* (Clarendon, Oxford, 2001).
- [32] G. P. Srivastava, *The Physics of Phonons* (Taylor & Francis, New York, 1990).
- [33] L. Lindsay, D. A. Broido, and T. L. Reinecke, *Phys. Rev. B* **87**, 165201 (2013).
- [34] N. Mingo, K. Esfarjani, D. A. Broido, and D. A. Stewart, *Phys. Rev. B* **81**, 045408 (2010).
- [35] C. A. Polanco and L. Lindsay, *Phys. Rev. B* **97**, 014303 (2018).
- [36] P. Giannozzi, S. Baroni, N. Bonini, M. Calandra, R. Car, C. Cavazzoni, D. Ceresoli, G. L. Chiarotti, M. Cococcioni, I. Dabo, A. D. Corso, S. de Gironcoli, S. Fabris, G. Fratesi, R. Gebauer, U. Gerstmann, C. Gougoussis, A. Kokalj, M. Lazzeri, L. Martin-Samos *et al.*, *J. Phys. Condens. Matter* **21**, 395502 (2009).
- [37] J. P. Perdew and A. Zunger, *Phys. Rev. B* **23**, 5048 (1981).
- [38] K. Esfarjani and H. T. Stokes, *Phys. Rev. B* **77**, 144112 (2008).
- [39] T. R. Anthony, W. F. Banholzer, J. F. Fleischer, L. Wei, P. K. Kuo, R. L. Thomas, and R. W. Pryor, *Phys. Rev. B* **42**, 1104 (1990).
- [40] S. Chen, Q. Wu, C. Mishra, J. Kang, H. Zhang, K. Cho, W. Cai, A. A. Balandin, and R. S. Ruoff, *Nat. Mater.* **11**, 203 (2012).
- [41] N. A. Katcho, J. Carrete, W. Li, and N. Mingo, *Phys. Rev. B* **90**, 094117 (2014).
- [42] A. Katre, J. Carrete, B. Dongre, G. K. H. Madsen, and N. Mingo, *Phys. Rev. Lett.* **119**, 075902 (2017).
- [43] K. I. Portnoi, V. M. Romashov, V. M. Chubarov, M. K. Levinskaya, and S. E. Salibekov, *Powder Metallurgy and Metal Ceramics* **6**, 99 (1967).
- [44] R. Naslain and J. S. Kasper, *J. Solid State Chem.* **1**, 150 (1970).
- [45] H. B. Borgstedt and C. Guminski, *J. Phase Equilib.* **24**, 572 (2003).
- [46] J. S. Kang, H. Wu, and Y. Hu, *Nano Lett.* **17**, 7507 (2017).
- [47] C. Whiteley, Y. Zhang, Y. Gong, S. Bakalova, A. Mayo, J. Edgar, and M. Kuball, *J. Cryst. Growth* **318**, 553 (2011).
- [48] <http://energy.gov/downloads/doe-public-access-plan>.